Renewable Energy 276 (2026) 126332

Contents lists available at ScienceDirect

Renewable Energy

journal homepage: www.elsevier.com/locate/renene

Experimental and numerical characterization of a large-stroke winch-based power take-off for wave energy converters

Wen-Yang Hsu [a,*], Yi-Hsiang Yu [b], Yu-Chi Chang [c], Lei Zuo [d], Yang-Chi Chung [c], Bo-Han Wang [c]

[a] Department of Harbor and River Engineering, National Taiwan Ocean University, Taiwan, ROC
[b] Department of Civil Engineering, National Yang Ming Chiao Tung University, Taiwan, ROC
[c] Green Energy and Environment Research Laboratories, Industrial Technology Research Institute, Taiwan, ROC
[d] Department of Naval Architecture and Marine Engineering, University of Michigan, Ann Arbor, MI, USA

ABSTRACT

Point absorber wave energy converters face critical survivability and efficiency challenges due to limited stroke constraints and destructive end-stop collisions in extreme seas. This study presents a 1 kW-scale winch-driven power take-off system with a 10 m active stroke, designed to geometrically decouple the internal drivetrain from constrained motion rails. To evaluate the drivetrain without hydrodynamic uncertainty, land-based crane trials imposed repeatable 10 m tether displacements, while the prescribed 1 m/s line velocity was selected to be broadly consistent with a 1:6 Froude-scaled representation of full-scale extreme vertical motion. The controlled actuation isolated the internal energy cascade and enabled stage-wise separation of speed-dependent mechanical losses from load-dependent electromagnetic losses across resistive loads of 4.5 to 45 Ω. Experiments identified an optimal internal conversion efficiency near 18 Ω, beyond which high-current effects degraded performance. Diagnostic analysis further showed that constant-parameter generator predictions failed when stator current exceeded the 5.16 A rated limit, causing over-predictions of current, torque, and electrical power due to armature reaction and magnetic saturation. To capture this behavior, a multi-domain physics-based model combined a no-load-calibrated viscous rotational damper with a current-dependent back electromotive force coefficient roll-off profile. This correction eliminated high-current prediction bias and restored agreement across the mechanical-to-electrical energy cascade. These findings demonstrate that single-point static tuning is insufficient under transient overloads. The validated model supports future upscaling and parameter-scheduled load control to maintain optimal operation, mitigate saturation, and maximize wave-to-wire energy extraction in irregular seas.

1. Introduction

The global pursuit of a decarbonized energy future highlights the need for diverse renewable sources, among which wave energy conversion (WEC) stands out for its high power density and predictability [1]. A wide variety of WEC designs have been proposed [2], yet large-scale commercial deployment remains constrained, with most concepts currently undergoing initial field trials or pilot-scale sea testing. Among these floating technologies, the point absorber (PA-WEC) has emerged as a leading configuration due to its compact footprint, omnidirectional response, and modularity [3,4]. This adaptability also makes PA-WECs highly suitable for the emerging strategic trend of co-locating WECs with floating offshore wind turbines [5], which is an integrated approach that helps reduce the overall Levelized Cost of Energy (LCOE) through shared infrastructure and optimized operations.

The PA-WEC design spectrum is typically defined by several key dimensions that allow for optimization across varying wave climates and water depths. Structural configurations range from simple single-buoy design [6,7], which aim for cost-effectiveness, to complex multi-buoy configurations [8,9], which are engineered to maximize energy absorption through relative motion between linked floaters. These systems vary in operational complexity, spanning from a single degree of freedom (DOF) to sophisticated designs that capture energy across multiple DOFs to optimize wide-band efficiency [10]. Furthermore, adaptability to the marine environment is achieved through various deployment methods, including floating surface units for co-location scenarios and fully submerged pressure-differential designs that prioritize survivability and operate independently of the water surface [11,12]. Finally, a wide range of power take-off (PTO) systems is employed, including high-efficiency direct-drive linear generators, robust hydraulic mechanisms, and mechanical transmission systems, each offering distinct trade-offs in power density and control complexity [13]. Despite this immense design diversity, all PA-WEC systems face a fundamental, unifying challenge: the critical trade-off between maximizing resonance-based energy capture in moderate seas and ensuring

* Corresponding author. No.2, Beining Rd., Zhongzheng Dist., Keelung City, 202301, Taiwan, ROC.
E-mail address: wyhsu@mail.ntou.edu.tw (W.-Y. Hsu).

https://doi.org/10.1016/j.renene.2026.126332
Received 18 April 2026; Received in revised form 5 July 2026; Accepted 17 August 2026
Available online 18 August 2026

robust survivability in extreme storm conditions [14,15].

In highly energetic and long-wave conditions, hydrodynamic theory suggests that the floating bodies of PA-WECs behave as passive followers [16,17] with a heave Response Amplitude Operator (RAO) approaching unity. For example, in a 50-year extreme sea state characterized by a significant wave height of $H_s = 12.7$ m and a peak period of $T_p = 11.8$ s [18], Airy wave theory dictates a maximum vertical surface velocity of approximately 3.3 m/s with heave and surge excursions exceeding 10 m. Consequently, the internal PTO driveline must physically accommodate kinematics exceeding 3.3 m/s at full scale. However, because most buoy dimensions are optimized for resonance, accommodating long internal motion rails conflicts with their constrained geometry. Many current designs employ limited-stroke PTOs (ranging from 0.3 to 5 m) equipped with spring-dampers or mechanical end-stops [13,19–21]. Recent investigations [6,21,22] have identified these rigid end-stop mechanisms as a critical vulnerability. When a massive wave drives the PTO beyond its physical stroke limit, the sudden deceleration induces massive impulsive snap loads, compromising the structural hull and accelerating mooring fatigue. Stroke limitation is thus recognized as a primary failure mode for floating PA-WECs.

To resolve these limitations, the winch-based PTO systems utilizing tethers have emerged as a promising alternative, as demonstrated by devices such as the Bolt Lifesaver [22], WaveSub [23], CalWave [24], and OscillaPower [25]. By geometrically decoupling the stroke length from the PTO housing, winch-based systems can theoretically accommodate the large-amplitude motions induced by extreme waves, thereby eliminating end-stop collisions and damping snap loads through the tether's compliance. However, evaluating the wide dynamic range of these systems presents a significant experimental challenge. Although open-sea trials [26] provide the most realistic wave-induced hydrodynamic forcing, they are costly, time-consuming, and constrained by uncontrollable weather conditions. Similarly, scaled wave tank experiments are often limited by facility dimensions and the achievable range of sea states. To overcome these challenges, land-based PTO testing using mechanical actuators, such as crane-driven setups or dry test rigs [27], has become a valuable methodology for controlled PTO evaluation. Although this dry-testing approach inherently decouples the PTO from complex wave-hydrodynamic interactions, it offers a distinct analytical advantage by effectively isolating the internal electromechanical dynamics. By removing hydrodynamic uncertainties, actuator-driven testing enables highly repeatable performance characterization, allowing researchers to precisely quantify mechanical friction, damping sensitivity, and energy conversion tradeoffs [28,29]. This controlled, decoupled parameter identification is an essential prerequisite for developing robust, high-fidelity wave-to-wire numerical models [30]. It ensures that the fundamental electromechanical behavior of the PTO is well understood and validated before introducing the compounding complexities of real ocean deployments.

Despite these advantages, research on large-stroke winch-based PA-WECs remains limited. The complex dynamic load distribution between the pretension-maintaining subsystem and the energy-extracting generator remains insufficiently explored. Furthermore, the rigorous identification of the power cascade efficiency through kW-scale integrated testing has not yet been systematically documented for platforms capable of 10 m strokes at high operating velocities. This gap is exacerbated by the reliance of many existing numerical tools on empirical Look-Up Tables (LUTs) [31] or static coefficients [32] derived from nominal land-based tests. While LUT-based models are effective in steady-state laboratory conditions, they routinely fail to capture the highly coupled, nonlinear loss mechanisms triggered during transient extreme events. In scenarios involving heavy electrical loads or overspeed conditions, unmodeled physical phenomena such as speed-dependent mechanical churning and localized magnetic saturation can dominate the response, making physics-based modeling essential for credible performance and survival-load prediction.

This study addresses these gaps by implementing a physics-based multi-domain PTO model, rather than relying on purely empirical coefficients or look-up tables (LUTs), to establish a systematic modeling and identification framework for large-stroke, winch-driven PA-WECs. The primary contributions include: (1) generating a large-stroke experimental dataset for an integrated kW-scale winch-driven PA-WEC PTO using a crane-based test rig with 10 m controlled tether motion, thereby reproducing the high-speed tether kinematics associated with 50-year extreme sea states; (2) rigorously decoupling and calibrating speed-dependent mechanical transmission losses from load-dependent electromagnetic nonlinearities, including current-dependent back-EMF coefficient roll-off, through integrated open-circuit and resistive-load testing; and (3) developing and validating a structurally consistent physics-based PTO model that provides a predictive alternative to conventional LUT representations for future system upscaling and advanced control design.

The remainder of this paper is organized as follows: Section 2 details the PA-WEC system architecture and the experimental program for the land-based trials. Section 3 presents the experimental results, including controlled-stroke time histories and a stage-wise analysis of the cycle-integrated energy budget. Section 4 describes the development of the physics-based PTO model and its validation against the experimental datasets. Section 5 provides a design-oriented discussion on loss attribution along the energy cascade and outlines control projections enabled by the validated model. Finally, Section 6 summarizes the key findings and presents the conclusions of this work.

2. System overview and land-based test procedure

2.1. Subsystem architecture and power flow

The operating principle of the proposed winch-based PA-WEC involves harnessing wave-induced relative motion between the floating body and the seabed. A tether translates the buoy's heave, surge, and sway into axial line force and velocity, which is then transmitted to the PTO system featuring a 1 kW permanent magnet synchronous generator (PMSG).

The buoy is a cylindrical structure with an outer diameter of 150 cm, a height of 102 cm, and a draft of 67 cm, providing a total displacement of 1168 kg. It features a central hollow conduit to allow unobstructed tether passage. Fig. 1 illustrates the overall winch-based PA-WEC system, while Fig. 2 details its internal components. For the land-based system identification and PTO calibration presented in this study, the buoy serves primarily as a stationary structural frame. Consequently, the electromechanical characterizations regarding line tension, transmission efficiency, and electrical conversion remain decoupled from specific floater hydrodynamics.

2.1.1. Primary transmission: from external force to rotational torque

The kinetic energy capture begins with an external driving force, which is created by a crane for land-based trials in this study or provided by wave excitation in future tank tests. This force acts on the tether, which serves as the primary link between the environment and the winch drum. As a result, the tether translates linear motion into rotational motion.

A critical design parameter for the winch is the fleet angle, defined as the angle between the tether entering the guide sheave and the drum centerline. According to maritime standards [33,34], minimizing this angle is essential to prevent uneven spooling, accelerated wear, and bending fatigue. Floating applications are characterized by prevalent roll, pitch, and horizontal drift induced by waves. To mitigate the resulting dynamic fleet angles, the winch is mounted at the top of the floater, and the guide sheave is positioned centrally at the hull base. This vertical separation ensures the tether remains aligned within the central conduit, inherently minimizing the fleet angle throughout the operational stroke.

Moreover, a feature of the proposed winch-based PTO is its capacity

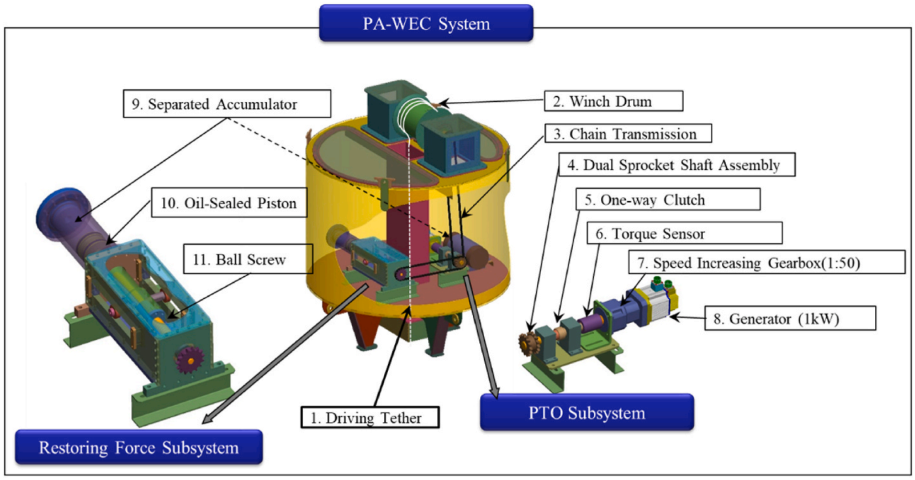

Fig. 1. 3D CAD rendering of the winch-based PA-WEC system, illustrating the primary modules: Winch Module, PTO Module, and the Restoring Force Module.

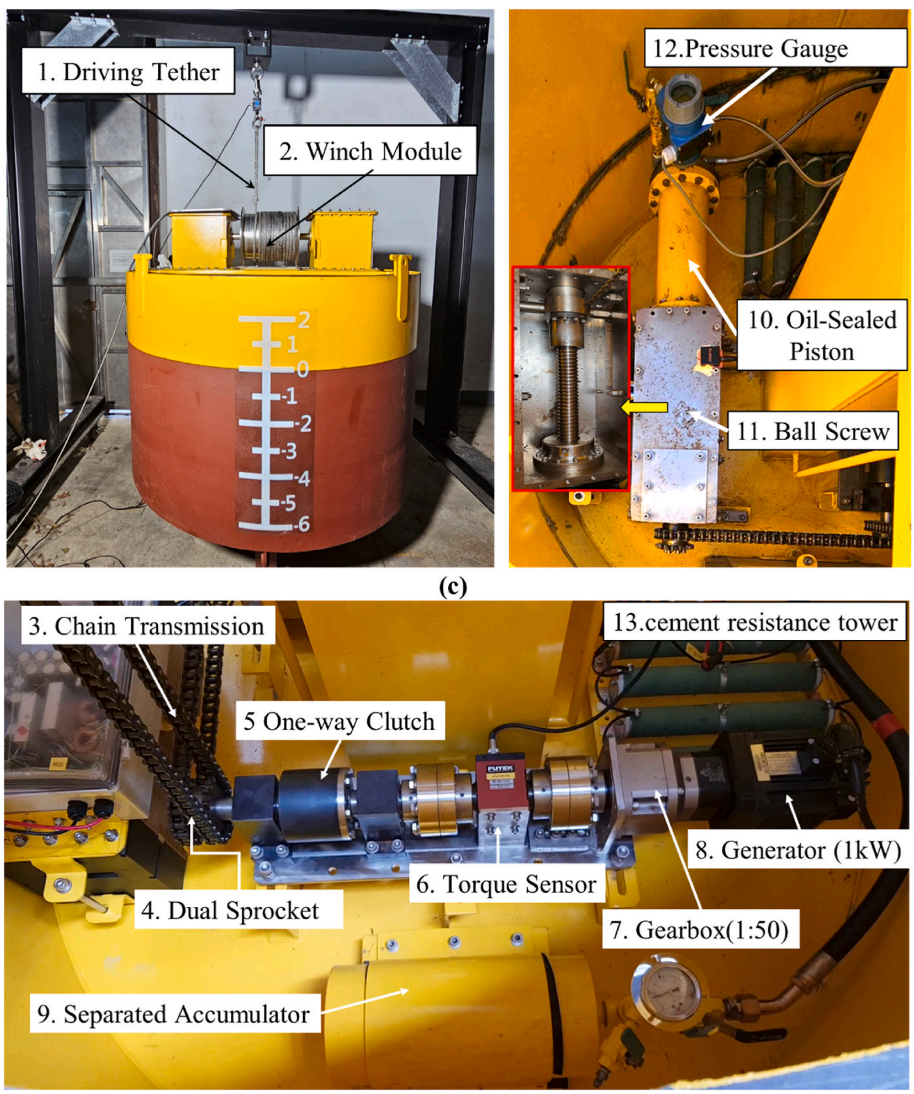

Fig. 2. Physical prototype of the winch-based PA-WEC. (a): External view of the cylindrical buoy and winch assembly mounted on the test frame. (b): Internal view of the restoring force module showing the pneumatic cylinder, ball screw, and pressure instrumentation. (c): Detailed view of the PTO drivetrain.

for exceptionally large strokes, which distinguishes it from traditional WEC designs constrained by linear guide rails or finite end-stop stroke limits. In this study, the PTO was characterized over a 10 m active stroke, facilitated by a 26 cm diameter winch drum. The relationship between the tether payout length (δ) and the drum's angular rotation (θ_{drum}) is governed by the drum radius ($r_{drum} = 0.13$ m):

$$\delta = \theta_{drum} \cdot r_{drum} \tag{1}$$

This high-capacity spooling capability ensures that the system remains operational in extreme sea states, providing a level of scalability that is difficult to achieve with linear-oscillator PTOs.

2.1.2. PTO and restoring force modules

The mechanical energy from the winch drum is transmitted via a central shaft to a drive chain, which descends to a dual sprocket assembly at the base of the hull. This double sprocket serves as the central mechanical junction, distributing the mechanical power into two co-located subsystems: the electrical PTO subsystem and the pneumatic restoring-force subsystem, as shown in Fig. 3.

The PTO subsystem is configured for unidirectional energy extraction, utilizing a one-way clutch to engage the powertrain only during the tether payout phase. This prevents high-inertia components from resisting haul-in motion, allowing for a faster transition to the trough phase in preparation for the next power generation cycle. Following the clutch, a torque sensor measures the mechanical input before it enters a 1:50 speed-increasing gearbox. This gearbox elevates the rotational speed to a range suitable for the 1 kW PMSG. The generated AC power is then processed through an AC/DC bus and dissipated across a cement resistance tower, allowing for passive control of PTO damping.

The restoring-force subsystem remains in constant engagement with the dual sprocket to ensure continuous tension management. This pathway utilizes a ball screw with a 10 mm lead to convert the rotational motion into linear travel, which drives a dual-chamber pneumatic cylinder along linear guide rails. This arrangement functions as a non-linear pneumatic spring, providing the necessary pretension to keep the tether taut during wave-induced reversals and to prevent destructive snap loads.

2.2. Land-based test facility and instrumentation

To evaluate the integrated electromechanical response of the PA-WEC under large-stroke conditions, an outdoor test campaign was conducted using a crane to prescribe vertical motion on the tether, thereby replicating the kinematic responses induced by the floating buoy's coupled heave and surge motions (as shown in Fig. 4). This setup provided a controlled environment to comprehensively validate the system's performance prior to ocean deployment, with a specific focus on mapping the full operational cycle. During the payout (lifting) phase, the primary objective was to quantify the stage-wise power flow and localize energy losses. By measuring the mechanical input power at the tether (P_{line}), the intermediate mechanical power upstream of the gearbox (P_{pto}), and the final electrical output at the load bank (P_{gen}), the cascade conversion efficiency can be quantified under varying resistive loads. This approach distinctly separates the mechanical friction losses of the primary drivetrain from the internal electromechanical losses of the PTO module. Conversely, the haul-in (lowering) phase provided an isolated condition to characterize the restoring-force dynamics. Because the one-way clutch mechanically disengages the generator during

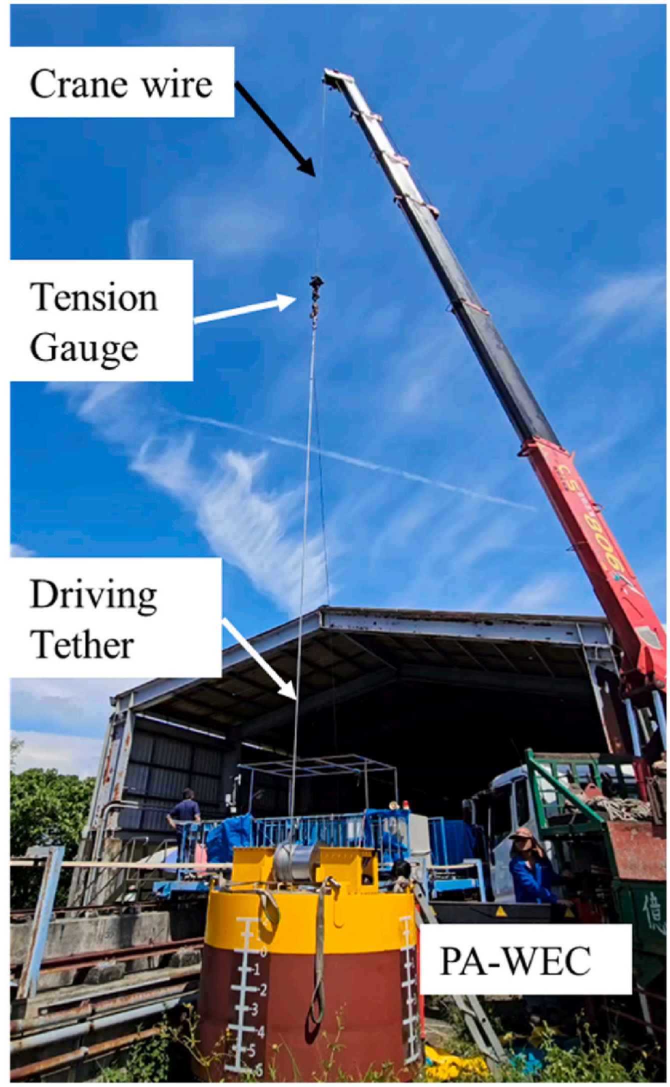

Fig. 4. Experimental configuration for the crane-based long stroke test.

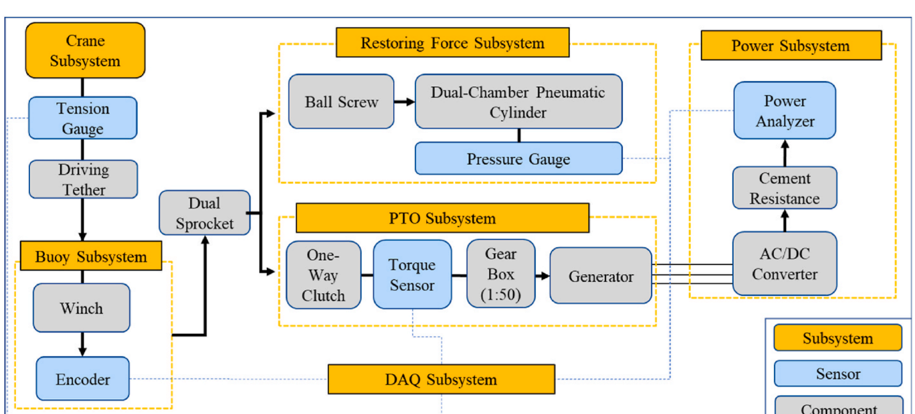

Fig. 3. Functional architecture and sensor integration of the PA-WEC system, showing the power cascade from the driving rope to the electrical load.

retraction, this phase allowed for the evaluation of the pneumatic system across its full 10 m displacement range. This isolated window enabled the verification of the pretension system's pressure-to-force linearity and the precise extraction of friction-related effects within the winch, completely free from electromagnetic damping influence.

Each trial followed a standardized motion profile. The crane lifted the 24 mm-diameter Dyneema tether from an initial displacement of 0 m to a peak stroke of approximately 10 m. This maximum elevation was maintained briefly to allow the PTO system to stabilize, after which the tether was lowered back to its initial position. To ensure repeatability and improve data reliability, the same motion cycle was repeated three times for each test configuration. The prescribed line velocity was selected based on Froude velocity scaling. For a representative 1:6 geometric scale, the velocity scaling factor is given by the square root of the length scale, yielding approximately 0.41. Applying this factor to the full-scale extreme vertical velocity of 3.3 m/s, as discussed in the Introduction, gives a corresponding scaled target velocity of approximately 1.3 m/s. Therefore, the 1 m/s line velocity used in the crane trials is physically reasonable and broadly consistent with Froude-scaled extreme-sea kinematics. This testing condition enables the PTO drivetrain to be evaluated under severe high-speed tether excursions while preserving repeatable, controlled actuation in a land-based environment.

During the lifting phase, the crane speed was prescribed to cover both the normal operating rotational range of the generator (up to 2000 RPM) and overspeed conditions, enabling the comprehensive evaluation of system performance under both nominal and extreme operating states. The experimental matrix comprised an open-circuit case and six discrete resistive loads: 45, 36, 27, 18, 9, and 4.5 Ω. For high-damping cases (9, and 4.5 Ω), the imposed crane speed was intentionally constrained to avoid excessively high generator currents. For each load, the test matrix produced repeatable time histories for line displacement (δ), line velocity (V_{line}), pneumatic pressure (p), line force (F_{line}), PTO shaft torque (τ_{pto}), line input power (P_{line}), PTO shaft power (P_{pto}) and final electrical power output (P_{gen}).

As established in the data acquisition framework, all data were captured at a synchronous 25 Hz sampling rate, ensuring time alignment between the tether-side mechanical input and the corresponding electrical output. Although this sampling rate cannot resolve high-frequency electromechanical transients, such as electrical ripple or local torsional vibration, the prescribed crane-driven excitations are low-frequency motions with characteristic periods of several seconds. Therefore, 25 Hz provides sufficient bandwidth to capture the dominant macroscopic drivetrain dynamics and support reliable cycle-averaged power calculations. Moreover, to ensure the fidelity of this experimental validation and isolate the root causes of system discrepancies, high-precision instrumentation was utilized across the test rig. Table 1 details the specifications, measurement ranges, and baseline uncertainties of the primary sensors. Because the maximum instrumental uncertainties are bounded within ± 0.2% of the full scale (F.S.), any large-scale divergence observed between the experimental data and the numerical model (e.g., in the over-speed regime) can be confidently attributed to unmodelled physical nonlinearities rather than measurement noise.

3. Experimental results

3.1. Time-domain dynamic response: representative case $R_L = 36\ \Omega$

In this section, we examine the measured full-system responses under a range of passive loadings. For brevity, a representative case ($R_L = 36\ \Omega$) is presented here to illustrate the phase-dependent dynamics and electromechanical coupling, while the cycle-integrated energy budgets and cascade efficiencies for all loads are subsequently summarized in Section 3.2.

As illustrated in the representative time histories (Fig. 5), the three repeated cycles demonstrate highly consistent phase-dependent responses in displacement, velocity, pressure, line force, shaft torque, and the three power channels. During the payout phase, the tether is pulled from 0 to 9.6 m, with a peak line velocity of approximately $V_{line} = 1$ m/s.

Over the same interval, the accumulator pressure increases passively from $20.5\ \mathrm{kg/cm^2}$ to $25.5\ \mathrm{kg/cm^2}$. Concurrently, the measured line force and PTO shaft torque rise rapidly and then stabilize at plateaus of roughly $F_{line} = 2.3$ kN and $\tau_{pto} = 310$ N·m, respectively. This indicates a strongly velocity-dependent electromechanical response during positive-velocity operation.

Correspondingly, the time-synchronous power traces exhibit clear plateau levels during payout. For this representative case, the mechanical line input power P_{line}, P_{mech} and P_{gen} reach approximate plateau values of 2.4 kW, 2.2 kW and 1.9 kW, respectively. The stage-wise power is computed as follows:

$$P_{line}(t) = F_{line}(t)V_{line}(t) \tag{2}$$

$$P_{mech}(t) = \tau_{pto}(t)\omega_{pto}(t) \tag{3}$$

$$P_{gen}(t) = V_{DC}(t)I_{DC}(t) \tag{4}$$

During the subsequent hold stage at maximum extension, V_{line} and all power terms approach zero, while the pneumatic pressure relaxes slightly from its peak value. The measured holding tension stabilizes at approximately 290 N with a small residual shaft torque (on the order of $\sim$1 N · m), which is consistent with the expected consistent with quasi-static effects near zero velocity.

During the haul-in phase, the V_{line} reaches approximately 1.27 m/s, while the generator is mechanically decoupled by the one-way clutch. As a result, the electrical power output remains near zero, yet the line tension remains positive and nearly steady at 175 N. This indicates that a sufficient minimum tension level is maintained during retraction. This behavior is of practical importance, as it effectively reduces the likelihood of slack events and potential snap loads during oscillatory operation under dynamic wave excitation. Furthermore, because this continuous pneumatic pretension keeps the tether taut, forming a compliant tensioned element that is sensitive to both external disturbances and internal drivetrain excitations. As observed in the F_{line} time histories, minor low-frequency fluctuations appear during rest or constant-velocity periods, likely originating from ambient wind or the crane's hydraulic micro-adjustments. Additionally, transient phases with large velocity gradients, such as sudden braking or motion reversals between payout and haul-in, induce distinct high-frequency oscillations. These oscillations may be attributed to transient excitation of the Dyneema tether's axial elasticity, coupled with mechanical chattering

Table 1
Specifications and measurement uncertainties of the primary experimental instrumentation.

Instrument	Manufacturer	Model	Range/Capacity	Resolution	Accuracy/Uncertainty
Tension Gauge	JIHSENSE	SL-2000	2000 kg	0.2 kg	±0.2% F.S.
Encoder	HENGXIANG OPTICAL	K100-C3V1024BQ35	Continuous	0.3515° (1024 Pulses Per Revolution)	±0.35°
Torque Sensor	FUTEK	TRS605	500 N ·m	Analog (DAQ limited)	±0.2% F.S.
Pressure Gauge	STAR METER	CYYZ18C	0 ∼ 20 MPa	Analog (DAQ limited)	±0.1% F.S.

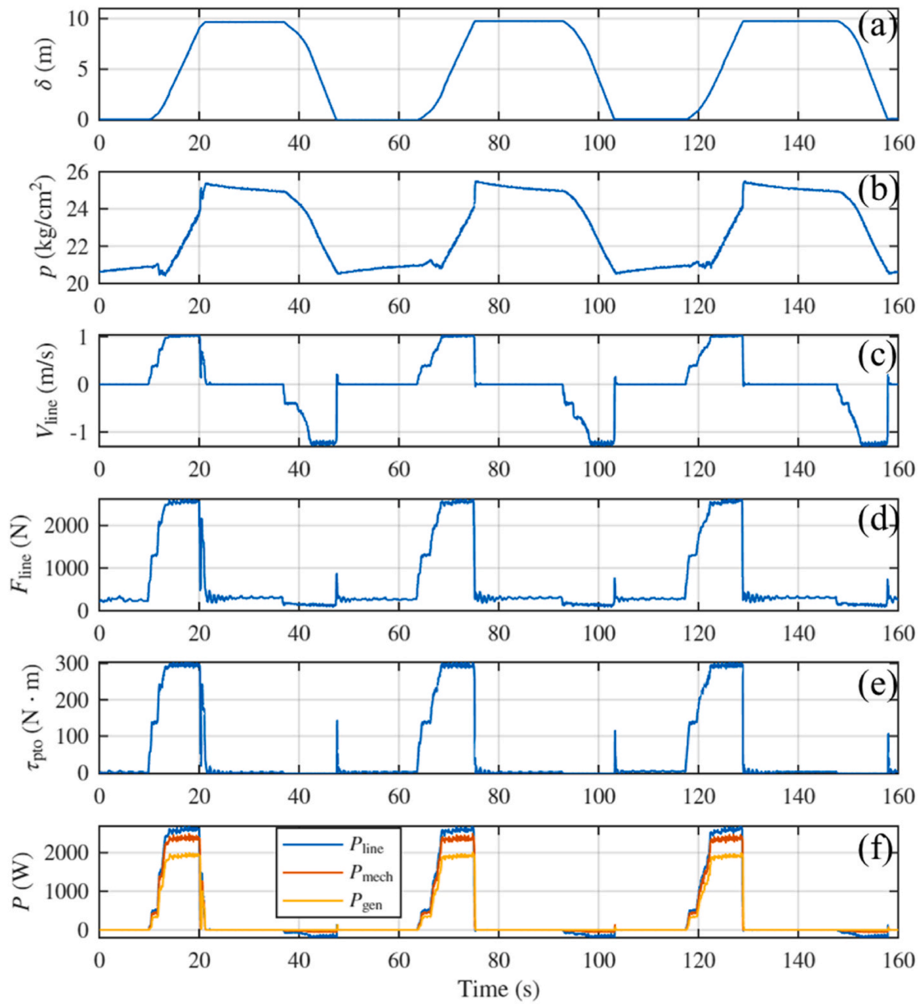

Fig. 5. Time histories from the crane-based full-system controlled-stroke test under a representative resistive electrical load ($R_L = 36\ \Omega$). (a) line displacement, (b) line velocity, (c) accumulator pressure, (d) line tension, (e) PTO shaft torque, and (f) line input power, PTO shaft power, and DC electrical output power.

associated with drivetrain backlash and one-way clutch transition dynamics.

3.2. Cycle-integrated energy budget and cascade efficiencies

Building on the time-domain responses presented in Section 3.1, this section quantifies how the measured power streams (P_{line}, P_{pto}, and P_{gen}) translate into cycle-integrated work and stage-wise (cascade) efficiencies. The objective is to distinctly separate (i) the mechanical transmission losses between the tether and the PTO shaft and (ii) the internal electromechanical losses between the PTO shaft and the DC output, thereby providing a consistent efficiency metric across all resistive load conditions.

Fig. 6 presents the measured power traces in both the time and rotational speed (RPM) domains for the first repeated cycle. The cycle-integrated energy over a selected phase window is defined as follows:

$$E_n = \int_{t_n^{(1)}}^{t_n^{(2)}} P(t)dt \tag{5}$$

where n denotes the n-th repeated cycle, and (1) and (2) indicate the start and end times of the phase of interest.

In this study, the payout integration window is defined from the instant when the line velocity first exceeds $V_{line} > 0.03$ m/s (payout onset) to a cutoff time shortly after the payout speed reaches its quasi-steady plateau, as shown in Fig. 6a. The cutoff is selected to (i) exclude the abrupt stop/termination transient at the end of the commanded stroke, and (ii) prevent the long plateau segment from dominating the integrated metrics and masking the initial acceleration behavior. To complement the window-based cycle integrals, payout-only data are also examined in the RPM domain (Fig. 6b), which provides an operating-point view of the same power streams and supports subsequent model validation. To extract the underlying operational tendency from the inherently oscillatory instantaneous measurements, a binned mean approach is applied to the RPM-domain data. The oscillatory power points are discretized into 100 RPM bins based on their corresponding generator speed. Within each bin, the average power is computed to construct a representative solid trend line, clearly visualizing the macroscopic characteristic curves. For each cycle n, stage-wise efficiencies are computed from the corresponding integrated energies as follows:

$$\eta_{trans,n} = \frac{E_{mech,n}}{E_{line,n}}, \eta_{gen,n} = \frac{E_{gen,n}}{E_{mech,n}}, \eta_{pto,n} = \frac{E_{gen,n}}{E_{line,n}} \tag{6}$$

To quantify the repeatability across the N repeated cycles, the ensemble mean ($\langle \eta \rangle$) for any given metric η_n is defined as:

$$\langle \eta \rangle = \frac{1}{N} \sum_{n=1}^{N} \eta_n \tag{7}$$

To avoid over-interpreting the small ensemble size (N = 3), the repeatability of the experiments was evaluated using the maximum

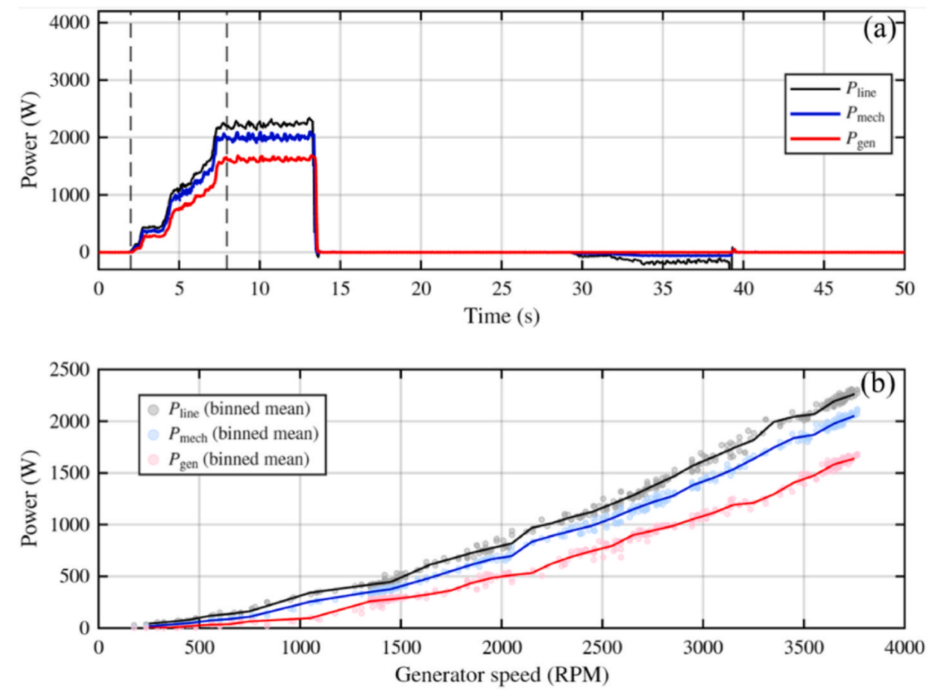

Fig. 6. Power-channel measurements under a representative resistive load ($R_L = 36\ \Omega$). (a) time histories of P_{line}, P_{mech}, and P_{gen} for a representative controlled-stroke cycle; dashed lines indicate the selected payout integration window. (b) payout-only data plotted versus generator speed, with solid lines representing the binned mean trends.

percentage deviation from the ensemble mean rather than treating the standard deviation as a rigorous uncertainty estimate. Across all repeated trials, the cycle-averaged energy $\langle E \rangle$ and power $\langle P \rangle$ exhibited a maximum deviation of 18%, reflecting the sensitivity of integrated power to transient start/stop dynamics and small variations in the prescribed crane motion. In contrast, the corresponding cascade efficiencies were much more repeatable, with a maximum deviation of only 2.5%. This indicates that although the absolute power level is affected by run-to-run dynamic variability, the relative energy-conversion behavior of the PTO system remains highly consistent across repeated tests.

For the representative 36 Ω load, the cycle-averaged powers and efficiencies are computed from the ensemble mean of three repeated payout cycles (Fig. 6). The mean line-input power is 1300 W and the PTO shaft power is 1169 W, yielding a mechanical transmission efficiency of 0.898. The DC electrical output power is 982 W, resulting in an electromechanical efficiency of 0.771. It is crucial to note that this value represents the internal mechanical-to-electrical conversion efficiency of the PTO driveline, entirely independent of the hydrodynamic wave-to-mechanical capture efficiency. This means 69% of the mechanical input is successfully converted to electrical power, while 31% is dissipated through internal mechanical and electromechanical losses.

Extending this analysis, Table 2 details the cycle-averaged powers and efficiencies across all resistive loads. Note that for heavy loads (9 Ω and 4.5 Ω), payout RPM was intentionally constrained to maintain safe current limits. To provide an intuitive comparison, Fig. 7a and b visualizes the power generation and efficiency trends, respectively. As shown in Fig. 7a, the stage-wise powers increase as the resistance decreases from 45 Ω to 18 Ω, reaching a distinct maximum at 18 Ω, before declining under lower-resistance loading. It should be noted that this decline is influenced not only by increased electrical damping, but also by the intentionally reduced operating speed imposed for the 9 Ω and 4.5 Ω cases. Fig. 7b illustrates the competing cascade losses. Mechanical efficiency steadily improves with lower resistance because parasitic mechanical losses become proportionally smaller at higher transmitted torques. In contrast, electromechanical efficiency remains relatively stable between 45 Ω and 18 Ω, but decreases markedly at 9 Ω and 4.5 Ω

Table 2
Payout energy budget and cascade efficiencies for all resistive-load cases.

Load R_L (Ω)	$\langle E_{line} \rangle$ (J) & $\langle P_{line} \rangle$ (W)	$\langle E_{mech} \rangle$ (J) & $\langle P_{mech} \rangle$ (W)	$\langle E_{gen} \rangle$ (J) & $\langle P_{gen} \rangle$ (W)	$\langle \eta_{trans} \rangle$	$\langle \eta_{gen} \rangle$	$\langle \eta_{pto} \rangle$
45 Ω	5937 (1083)	5222 (953)	3988 (728)	0.879	0.763	0.671
36 Ω	7123 (1300)	6407 (1169)	4947 (903)	0.898	0.771	0.693
27 Ω	8616 (1446)	7898 (1325)	6119 (1027)	0.915	0.773	0.707
18 Ω	11,738 (1969)	11,080 (1859)	8576 (1439)	0.944	0.774	0.730
9Ω	7621 (1279)	7275 (1221)	5311 (891)	0.955	0.730	0.697
4.5 Ω	4820 (809)	4618 (775)	2898 (486)	0.958	0.627	0.600

due to current-dependent copper losses and magnetic saturation. Consequently, the overall cascade efficiency exhibits a peaked trend, with the optimum occurring near 18 Ω. These results indicate that moderate resistive loading, particularly within the 27–18 Ω range, provides the most favorable balance between power extraction and electrical conversion losses.

4. Physics-based numerical model and validation

Section 4 presents a physics-based numerical representation of the onshore PTO system and validates it against the experimental datasets reported in Section 3. To comprehensively capture the system's behavior, this modeling effort focuses on several core objectives. Primarily, it aims to reproduce the measured phase-dependent tether dynamics (payout, hold, and haul-in) under long-stroke motion, explicitly including the asymmetric engagement behavior introduced by the one-way clutch. Furthermore, the model seeks to capture the operating-point dependence of the generator torque, DC voltage, current, and power under discrete resistive loads. Ultimately, this framework evaluates how

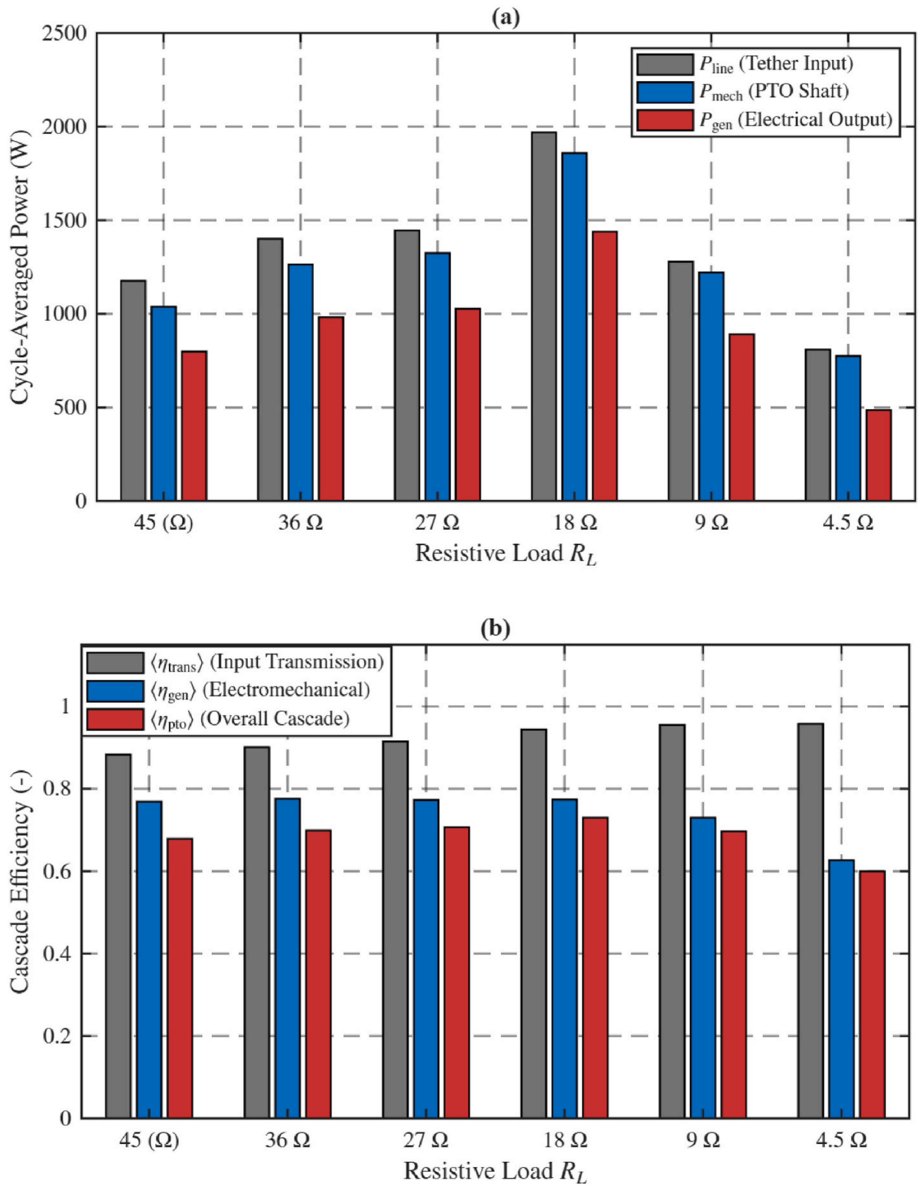

Fig. 7. Cycle-averaged power and cascade efficiency distributions across the tested resistive-load matrix. (a) Comparison of stage-wise power, showcasing 18 Ω as the optimal impedance configuration for maximizing power extraction. (b) Distribution of cascade efficiencies, illustrating the competing nature of mechanical and electrical losses and confirming that moderate loading yields the optimum overall efficiency.

accurately a specification-initialized, physics-based model, which is constructed primarily from subsystem supplier parameters rather than empirically fitted Look-Up Tables (LUTs), can predict PTO behavior, particularly in the diagnostic range from rated to overspeed conditions. This final objective is crucial for design-stage assessment and future scaling. Unlike LUT-based representations, which typically require extensive empirical re-testing when hardware is modified, a physically coupled model provides a structurally consistent baseline for adapting specific physical parameters.

However, it must be acknowledged that a purely specification-driven modeling approach is inherently limited. Critical system-specific parameters, such as assembly-dependent friction losses, transmission compliance, and current-dependent back-EMF coefficient roll-off under heavy electrical loading or overspeed operation, are not provided by component suppliers. These parameters may vary nonlinearly with speed, load, current, and assembly conditions. Therefore, while the physics-based numerical model provides a useful analytical tool for exploring broad parameter variations during the design phase, it cannot fully replace physical prototype evaluation. Comprehensive land testing remains indispensable for empirically calibrating unmodeled parasitic losses and identifying complex electromechanical nonlinearities prior to ocean deployment.

4.1. Subsystem models and coupling strategy (physics-based PTO model)

4.1.1. Overall PTO modelling framework

To interpret the land-based test results and establish a physics-based PTO representation, a multi-domain model was developed in MATLAB/Simscape [35]. Fig. 8 presents the complete physics-based PTO model architecture. The model follows the physical drivetrain topology and is driven by a prescribed V_{line} input, which is derived from the experiment in Section 3 and applied through a velocity source to impose the payout, hold, and haul-in phases. The imposed tether velocity is converted to rotational motion in the winch block and coupled to a rotational inertia representing the reflected inertia of the drum and drivetrain. The tether-coupled dynamics are represented by two subsystems: a

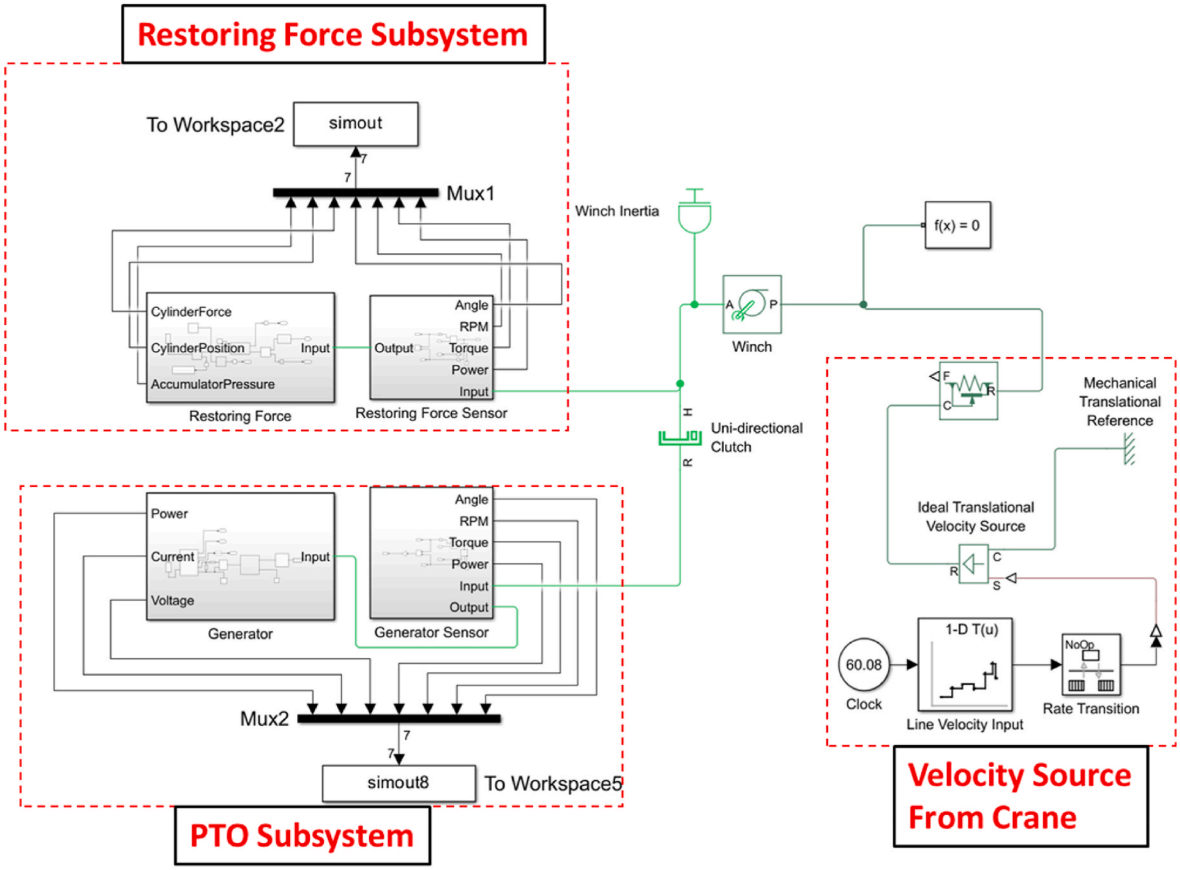

Fig. 8. Overall physics-based PTO model for land-based tests, driven by a prescribed line-velocity input and comprising a restoring-force subsystem and a PTO subsystem coupled through a one-way clutch.

restoring-force subsystem that provides compliant pretension, and a generator subsystem connected through a one-way clutch. The clutch engages during payout (positive line velocity) to transmit torque to the generator and disengages during haul-in to decouple the generator's inertia and electromagnetic resistance from the retraction load.

4.1.2. Restoring-force subsystem

The restoring-force subsystem represents the tether-coupled compliance and pretension mechanism that maintains positive line tension throughout operation, thereby reducing the likelihood of slack events and supporting stable drivetrain engagement. In the physical system, the restoring force is provided by a gas-charged accumulator coupled with a single-acting actuator (Fig. 9).

In the restoring force subsystem, the Isothermal Liquid (IL) library is applied. A leadscrew element provides the kinematic interface between the drivetrain and the fluid domain by converting rotational motion of the winch drum into the actuator's translational displacement. The leadscrew pitch and conversion efficiency govern the displacement

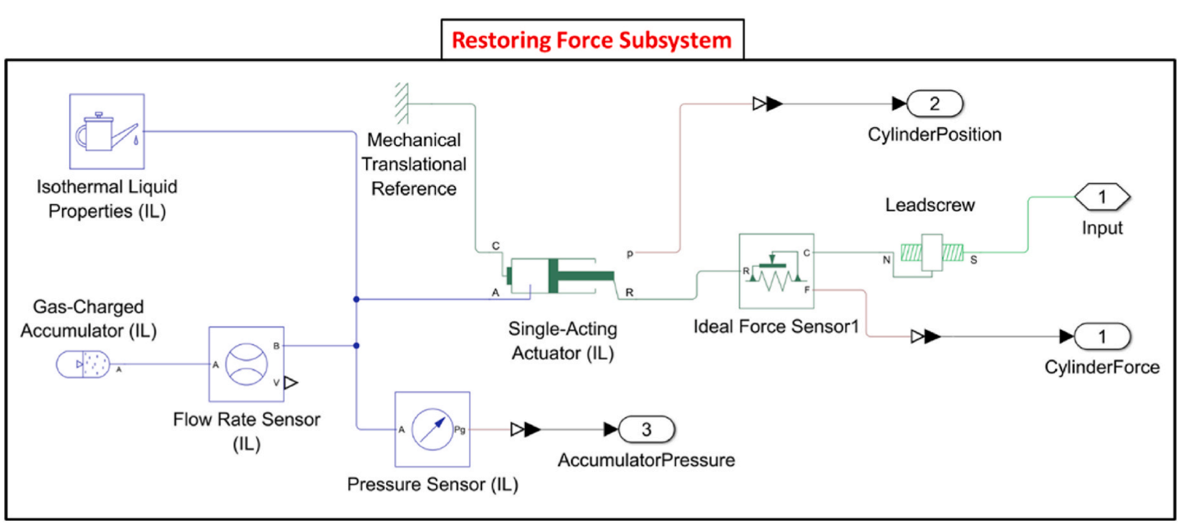

Fig. 9. Restoring force subsystem with a gas charged accumulator.

mapping between the mechanical and fluid subsystems. During payout, actuator extension drives fluid into the gas-charged accumulator, producing a nonlinear pressure increase as the gas volume decreases. The resulting pressure generates a displacement-dependent restoring force at the piston, which is transmitted back to the line side through the mechanical interface, yielding the progressive stiffness observed in the experiments.

For the gas-charged accumulator model, an isothermal process is assumed as a reasonable simplification. During a full 0–10 m stroke, the measured pressure in the 4 L accumulator varies only moderately, from approximately 21 to 25 kg/cm^2. Even under worst-case adiabatic compression, this limited pressure ratio would produce a theoretical temperature rise of approximately 15°C, corresponding to only a small thermal pressure deviation relative to the absolute operating pressure. Moreover, realistic ocean wave excitation is unlikely to impose repeated continuous full-stroke compression cycles; instead, the random intervals between large stroke events allow partial heat dissipation to the surrounding environment. Given these conditions, the isothermal assumption is considered sufficient for capturing the quasi-static restoring-force behavior of the pneumatic pretension subsystem without introducing unnecessary computational complexity.

Key block parameters that govern the restoring-force dynamics (actuator geometry, initial pressure, accumulator settings) and the kinematic interface (leadscrew lead and friction efficiency) are summarized in Table 3. The subsystem also includes virtual sensors for direct comparison with measurements: pressure and flow-rate sensors track the fluid-state evolution, while force and position signals record the actuator load and stroke. These outputs are used to quantify energy storage/release behavior and to inform calibration of loss effects reflected by the quasi-static hysteresis response.

4.1.3. Drivetrain and generator system

The drivetrain and generator subsystem converts the tether-coupled mechanical input into electrical power and provides the primary resistive torque during payout. As shown in Fig. 10, the rotational motion of the winch drum is transmitted through a gearbox with a 1:50 gear ratio and a constant efficiency ($\eta_{gear} = 0.9$) to a 1 kW PMSM. Additionally, a lumped rotational compliance element included to represent drivetrain elasticity. A one-way clutch is incorporated to capture the prototype's mechanical-rectification behavior: during payout ($V_{line} > 0$) the clutch engages and transmits torque to the generator, whereas during haul-in ($V_{line} < 0$) it disengages so that generator and gear inertia, together with electromagnetic resistance, do not contribute to the retraction load. This switching behavior is essential for reproducing the asymmetric force–velocity response observed in the long-stroke tests.

The electrical subsystem is modeled as an explicit physical network

Table 3
Key block parameters for the restoring-force subsystem and kinematic interface.

Component/Block	Parameter	Value	Unit
Single-Acting Actuator (IL)	Piston cross-sectional area	7850	mm^2
	Stroke	250	mm
	Initial piston displacement	200	mm
	Initial liquid pressure	21	bar
Accumulator (IL, gas-charged)	Precharge pressure	21	bar
Gas-Charged Accumulator	Total accumulator volume	4	L
Leadscrew (Mechanical Interface)	Lead	10	mm/rev
	Friction model	Constant efficiency	N/A
	Lead angle	5	deg
	Thread half angle	4.5	deg
	Friction coefficient	0.04	N/A

rather than a prescribed efficiency map. The PMSM generates three-phase AC power, which is rectified using a three-phase diode bridge and filtered by a DC-link capacitor (with an inductor included for smoothing) before being dissipated in an external resistive load. DC voltage, current, and power are monitored using a power analyzer block. By resolving the coupled electrical dynamics, the model captures the dependence of electromagnetic torque on rotational speed (via back-EMF) and on the applied resistive load, which can be interpreted on the mechanical side as an effective, load-dependent electromagnetic damping.

Key generator-subsystem parameters are summarized in Table 4. Unless otherwise noted, parameters were initialized based on supplier specifications using a constant-parameter PMSM formulation (constant L_d, L_q and PM flux), with the back-EMF constant K_e specified in the Simscape-compatible voltage definition. This specification-initialized configuration serves as a transparent baseline for the subsequent model–data comparisons and highlights operating conditions where unmodeled loss mechanisms may become influential.

4.2. Parameter identification and calibration using open-circuit tests

Although most subsystem parameters in the physics-based PTO model were initialized from manufacturer specifications, targeted calibration was performed using open-circuit crane trials of the full PA-WEC system. These tests minimize electromagnetic loading while preserving the integrated mechanical dynamics (e.g., inertia of drum and generator, mechanical losses of gearbox, and one-way clutch engagement) under long-stroke motion. Crucially, this open-circuit dataset serves a dual purpose: rigorously isolating speed-dependent mechanical losses for drivetrain calibration, and empirically identifying the generator back-EMF constant (K_e) that governs the speed–voltage relationship.

Because the electrical load torque is negligible during open-circuit operation, which was approximated in the simulation using a large 4500 Ω resistance, the measured line tension is predominantly governed by mechanical inertia, drivetrain friction, and pneumatic restoring forces. To calibrate the mechanical losses and address high-speed transmission dynamics, a lumped-parameter approach was adopted. First, the friction parameters of the leadscrew interface were empirically calibrated (As shown in the mechanical interface column of Table 3) to yield forward and reverse efficiencies of approximately $\eta_{forward} \approx 0.68$ and $\eta_{reverse} \approx 0.54$. This interface intentionally serves as a lumped representation for all mechanical parasitics within the restoring subsystem, accounting for piston seal friction, cylinder wall friction, and assembly misalignment. Second, to avoid the numerical stiffness associated with modeling discrete chain meshing, the drive chain and dual sprocket losses were aggregated into the adjacent rotary transmission blocks setting the constant gearbox efficiency to 0.95 and explicitly introducing a rotational viscous damper at the high-speed shaft. By matching the simulated high-speed line tension to the no-load measurements, a viscous damping coefficient of 0.00075 N m s/rad was identified. This mechanical calibration corrects the baseline tension response and separates mechanical parasitic losses from the electromechanical nonlinearities examined in the subsequent resistive-load simulations.

Transitioning to the electrical domain, Fig. 12 summarizes the open-circuit trials used to identify the back-EMF constant across three repeated cycles. Rather than using an arbitrary time window, the analysis strategically isolates the quasi-steady payout region by filtering the dataset for generator speeds exceeding 1000 RPM. This threshold is applied to exclude low-speed start-up transients, where poor signal-to-noise ratios and the non-linear forward voltage drops of the rectifier diodes can severely distort the linear parameter estimation. Under these filtered high-speed conditions, the measured DC current remains negligible ($I_{dc} < 0.1$ A, as shown in Fig. 12a), confirming a strict open-circuit state. Consequently, resistive load drops are completely negligible, and the measured DC bus voltage (V_{dc}) is dominated by the rectified generator back-EMF (Fig. 12b).

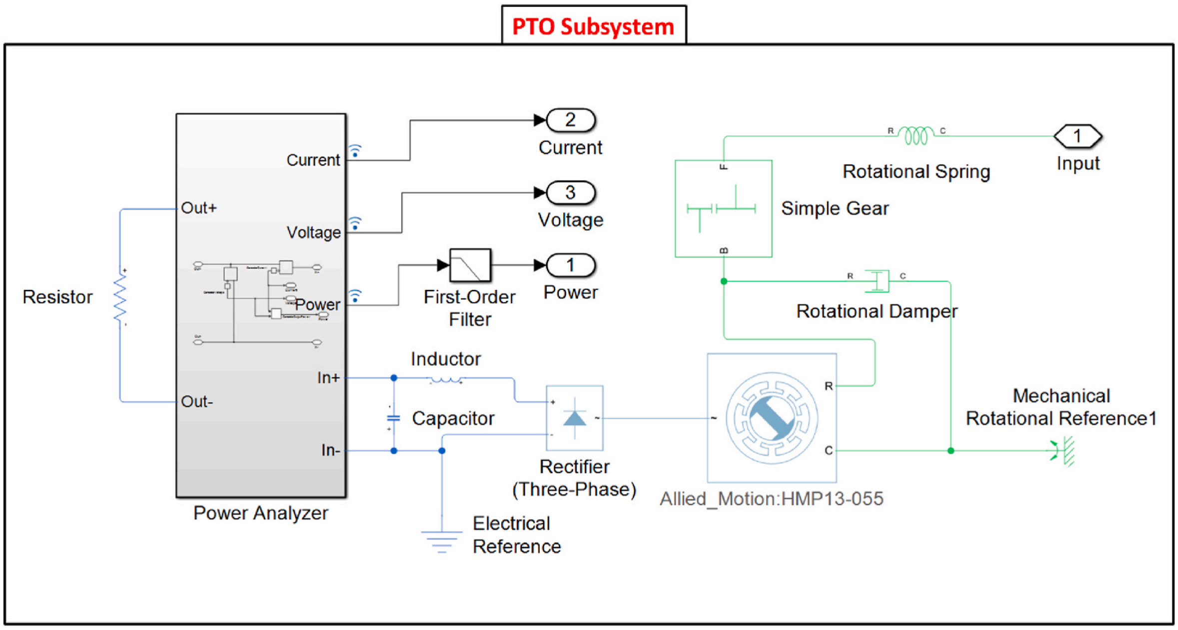

Fig. 10. Generator subsystem model including gear stage, PMSM, three-phase rectifier, DC-link filter, and resistive load.

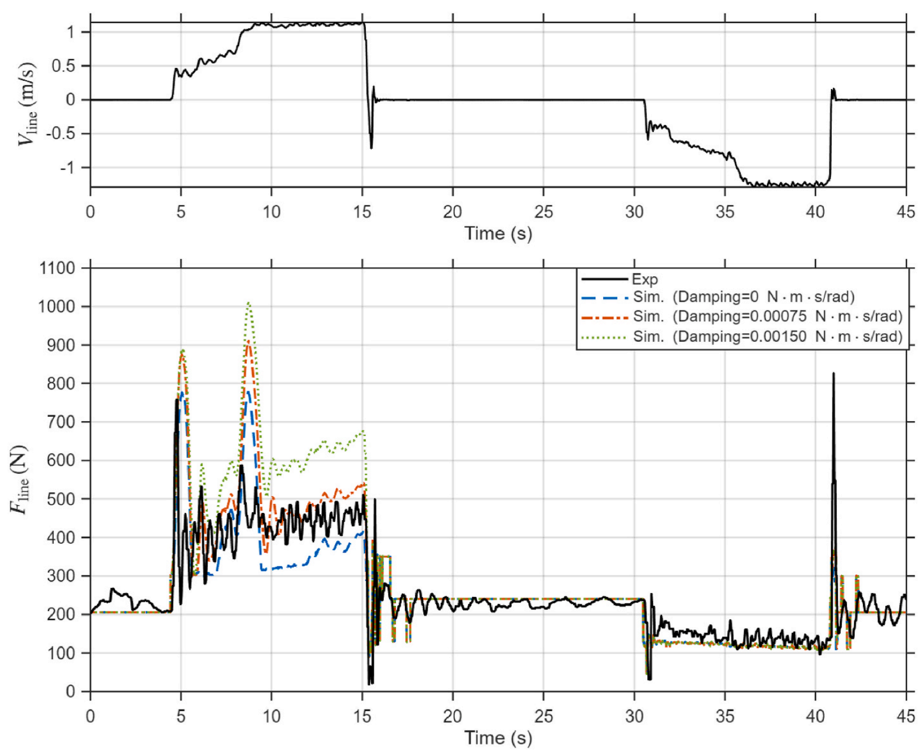

Fig. 11. Calibration of lumped mechanical losses (viscous damping, gearbox efficiency, and interface friction) using open-circuit trials. (top) V_{line}). (bottom) Measured versus simulated line tension (F_{line}) across varying rotational damping coefficients.

With a three-phase diode bridge and a DC-link capacitor, the capacitor charges to approximately the rectified line-to-line back-EMF peak minus two diode drops. Accordingly, the line-to-line RMS back-EMF is estimated from the measured DC voltage as:

$$V_{LL,rms} \approx \frac{V_{dc} + 2V_d}{\sqrt{2}} \tag{8}$$

where V_d is the forward drop of a single diode and two diodes conduct in the DC path of the bridge (here $V_d \approx 0.7$ V). Low-speed points were excluded because capacitor charging becomes intermittent and V_{dc} is no longer proportional to the back-EMF envelope. The reconstructed $V_{LL,rms}$ exhibits an approximately linear dependence on rotational speed over the selected operating range (Fig. 12c). The line-to-line RMS back-EMF constant is obtained from the slope of the linear regression:

$$K_{e,LL,rms} = \frac{V_{LL,rms}}{\omega} \text{ (V / rpm)} \tag{9}$$

Using Eq. (9), we yield $K_{e,LL,rms} = 0.0620$ V/rpm ($R^2 = 0.9805$). This

Table 4
Key parameters for the drivetrain–generator–rectifier subsystem in the PTO model.

Component/Block	Parameter (Symbol)	Value	Unit
Winch Inertia	Inertia	0.3	kg.m^2
Gear stage (Simple Gear)	Gear ratio	50	N/A
	Meshing efficiency	0.95	N/A
	Backlash	Disabled	N/A
Rotational Damper	Damping Coefficient	7.5 × 10^{-4}	N·m·s/rad
Rotational compliance (Rotational Spring)	Spring rate	2000	N·m/rad
PMSM (Allied Motion HMP13-055)	Pole pairs	2	N/A
	Back-EMF constant	0.0617	V/rpm
	Stator resistance per phase	0.61	Ω
	(d)-axis inductance	0.00335	H
	(q)-axis inductance	0.00335	H
	Iron-loss model	None	N/A
	Rotor inertia	6260	g·cm^2
	Rotor damping	0	N·m/(rad/s)
Rectifier + DC link	Three-phase rectifier	Diode bridge	N/A
External load	DC load resistance	45–4.5	Ω

fitted value agrees closely with the manufacturer reference value (0.0617, in Table 4) and lies within the ±10% tolerance bounds shown in Fig. 12c. For compatibility with the Simscape PMSM block, which parameterizes back-EMF using phase-to-neutral peak voltage, the line-to-line RMS quantity is converted using sinusoidal relationships:

$$V_{ph,peak} = V_{LL,rms}\frac{\sqrt{2}}{\sqrt{3}}, K_{e,ph,peak} = K_{e,LL,rms}\frac{\sqrt{2}}{\sqrt{3}} \tag{10}$$

Using the fitted value above gives $K_{e,ph,pk} = 0.0506$ V/rpm, which is used in the physics-based PTO model.

4.3. Model validation and discrepancy analysis under controlled-stroke tests

This section evaluates the baseline of physics-based PTO model, which is parameterized using manufacturer specifications, against experimental data from the controlled-stroke crane tests under resistive loading. We aim to assess how effectively the model captures the observed electromechanical trends and operating-point dependencies. Since the generator is rated for 1 kW at 2000 RPM, data obtained beyond this rated speed serves as an overspeed diagnostic range, highlighting model limitations and non-ideal physical behaviors.

4.3.1. Primary electromechanical observables versus speed (R_L = 18 Ω)

In the following, the 18 Ω resistive load is selected as the representative case for this detailed analysis because it yields the optimal overall cascade efficiency and allows the system to achieve its rated 1 kW electrical output at the nominal operating speed of 2000 RPM. Fig. 13 first compares the tether-coupled responses regarding the PTO and pretension dynamics for this specific loading condition. The pressure-displacement relationship in Fig. 13a is closely captured, suggesting that the restoring-force subsystem effectively accounts for the measured pressure rise over the full stroke. In Fig. 13b, the model successfully reproduces the qualitative transition between low-force haul-in and the strongly resistive payout system. However, deviations emerge at higher positive velocities, where the experimental line force increases less steeply than the simulation. Consistently, the DC power mapping in Fig. 13c shows that P_{dc} increases monotonically with RPM. While the

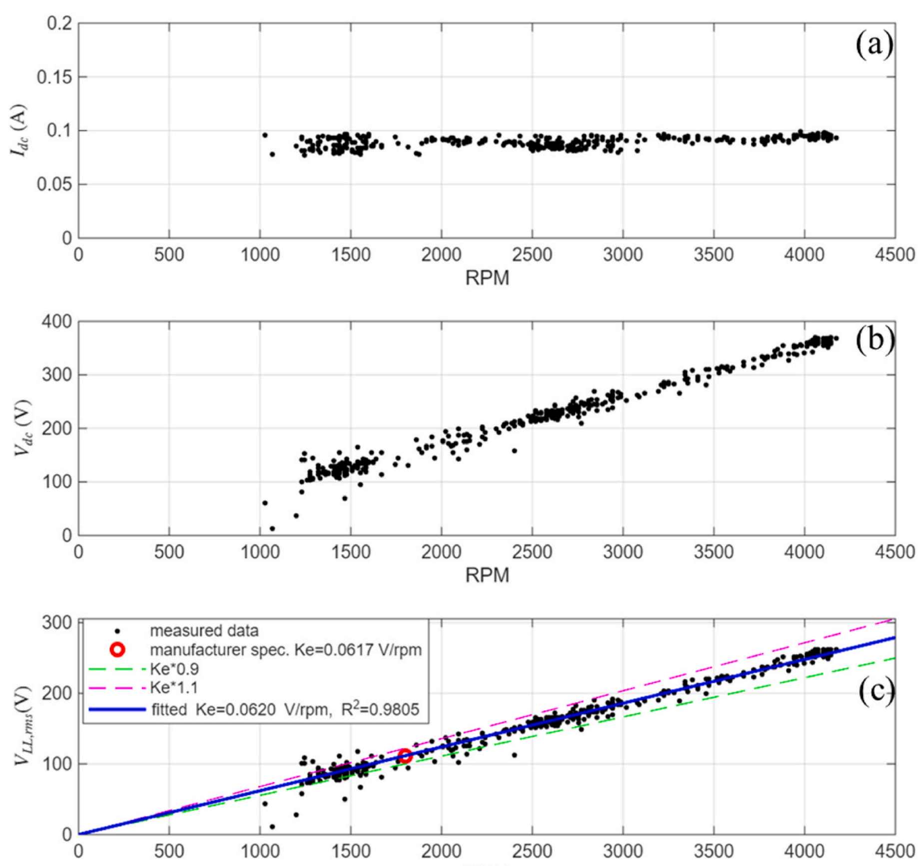

Fig. 12. Open-circuit crane data used to identify the back-EMF constant: (a) I_{dc} versus RPM, (b) V_{dc} versus RPM, and (c) reconstructed $V_{LL,rms}$ versus RPM, overlaid with the experimental linear fit and the manufacturer reference including ±10% bounds.

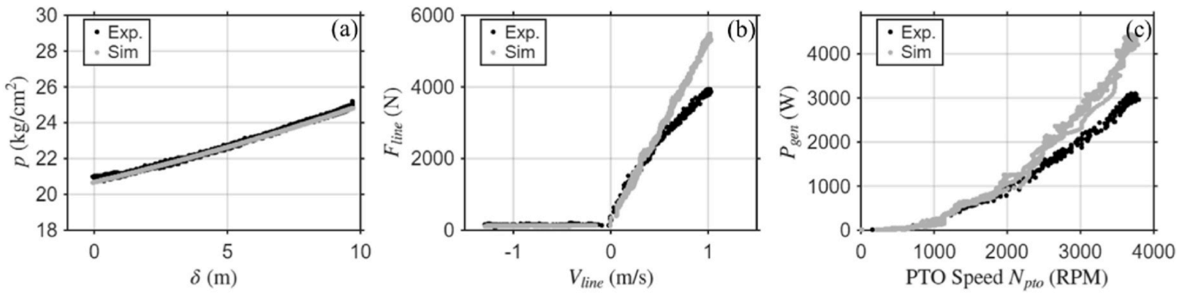

Fig. 13. Comparison between experimental measurements and simulation results for the 18 Ω load case: (a) pressure versus displacement (p versus δ), (b) line force versus line velocity (F_{line} versus V_{line}), and (c) DC power output (P_{gen}) versus generator speed.

model captures the overall curvature typical of a resistive load driven by speed-dependent back-EMF, it tends to overpredict P_{dc} in the diagnostic range from rated to overspeed conditions.

Fig. 14 compares generator-side observables against rotational speed for the same resistance load ($R_L = 18$ Ω). Although the model captures the overall monotonic trend, it systematically overpredicts τ_{shaft}, V_{dc}, and I_{dc} at high operating points, particularly above 2000 rpm (Fig. 14a–c). Interestingly, the apparent DC-side resistance R_L remains nearly constant at mid-to-high speeds and aligns well with the simulation (Fig. 14d). This suggests the discrepancy is not rooted in an incorrect external load value, but rather points to internal electromechanical losses or saturation effects that become more pronounced at high speeds and currents.

It is anticipated that under high-load operation, non-ideal effects, such as temperature-induced copper losses, diode-bridge conduction losses, and magnetic saturation, reduce the actual DC output. These findings suggest that incorporating a conservative loss augmentation (or effective parameter roll-off) could improve model agreement in the over-speed diagnostic range while maintaining accuracy within the primary operating window.

4.3.2. Loss-proxy analysis: identifying speed- and current-dependent discrepancies

To assess model fidelity across the full resistive-load matrix, Fig. 15 presents the binned-mean torque–speed characteristics on the generator side. The baseline model captures the expected monotonic trend and shows strong agreement under light-to-moderate loads (45 to 27 Ω) within the rated-speed region. However, a noticeable divergence emerges as the electrical loading intensifies (18 to 4.5 Ω) and within the overspeed diagnostic range (RPM > 2000), where the simulation consistently overpredicts torque. This deviation suggests that the mismatch stems from increasingly non-ideal electromechanical conversion at high operating points, rather than a simple error in the prescribed external load. To pinpoint the origin of this high-speed and high-load mismatch, we define an electrical-side loss proxy as:

$$P_{loss,elec} = P_{mech} - P_{gen} \tag{11}$$

Fig. 16 examines the behavior of this loss proxy against RPM for representative resistances spanning moderate to high current demands (e.g., 27, 18, and 9 Ω). In all cases, the magnitude of the loss proxy increases with RPM. This trend suggests that velocity-dependent parasitic mechanisms within the drivetrain, such as mechanical viscous drag, bearing windage, or oil churning, may contribute to the observed discrepancy. This observation aligns closely with recent literature; for instance, Dragić et al. [26] demonstrated in sea trials that mechanical PTOs suffer from substantial unmodelled sliding friction, while Henriques et al. [28] noted that such speed-dependent mechanical losses are inherently amplified in scaled experiments. Furthermore, as the resistance decreases (driving higher currents), the loss proxy rises further within comparable RPM ranges. This secondary trend points to superimposed current-dependent effects, such as copper losses, conduction losses in the rectifier and wiring, as well as potential electromechanical

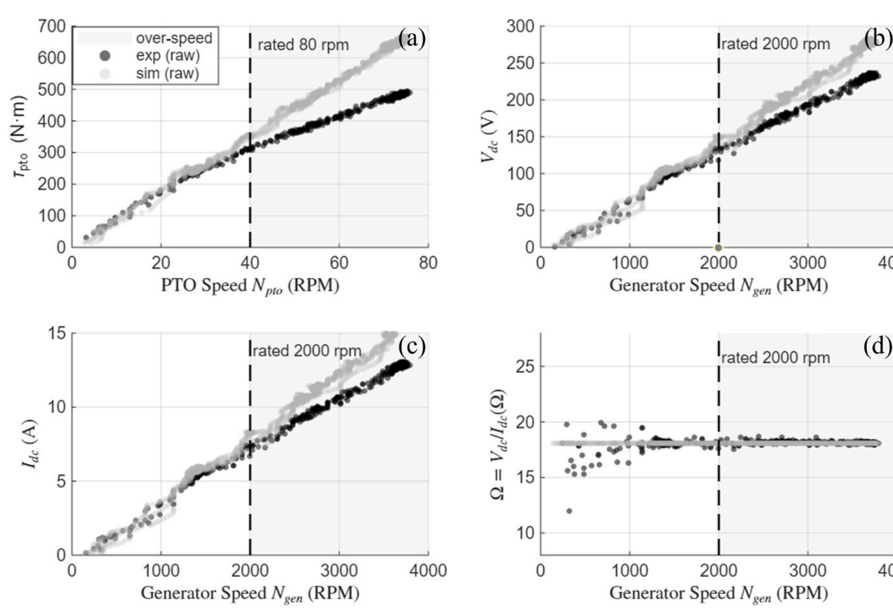

Fig. 14. Experimental–simulation comparison of generator-side observables versus RPM for $R_L = 18$ Ω: (a) shaft torque τ_{shafrt}, (b) DC voltage V_{dc}, (c) DC current I_{dc}, and (d) apparent DC resistance $\Omega = V_{dc}/ I_{dc}$. The shaded region indicates the over-speed diagnostic range.

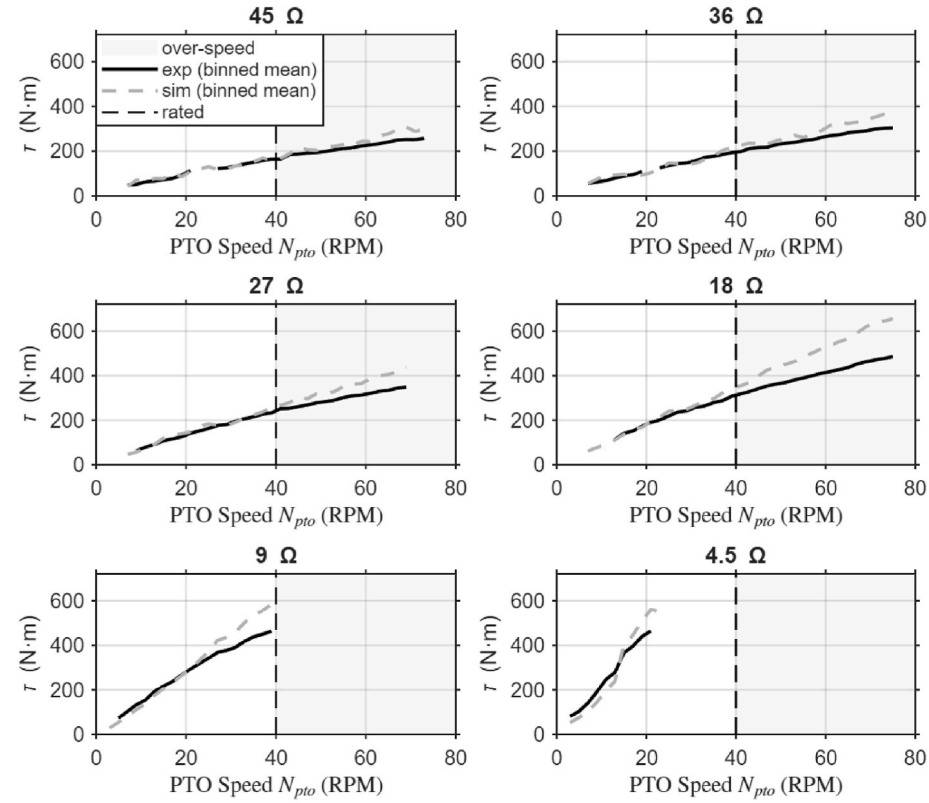

Fig. 15. Binned-mean torque-speed comparison (experiment versus simulation) for all resistive load cases (45, 36, 27, 18, 9, and 4.5 Ω). The dashed line indicates the rated speed at low speed shaft (40 RPM), and the shaded region denotes the overspeed diagnostic range.

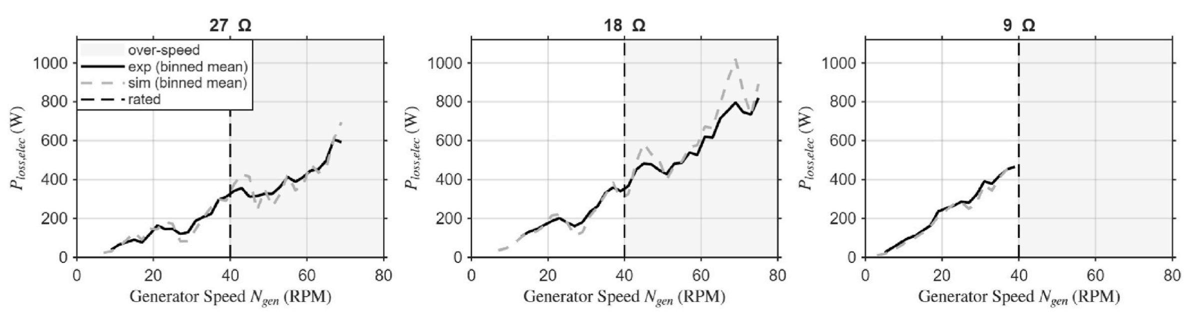

Fig. 16. Electrical-side loss proxy ($P_{loss,elec}$) versus RPM (binned mean) for representative loads (27, 18, and 9 Ω), comparing experiment and simulation. The dashed line indicates the rated speed (2000 RPM).

nonlinearities under heavy electrical loads. As investigated by Gaspar et al. [29] and recently highlighted by Yang et al. [36], the intrinsic nonlinearities introduced by electrical drive constraints and active mechanical transmissions under highly transient loads make the evaluation of achievable power exceedingly difficult. Further validating these intertwined effects, Fig. 17 presents the electrical-stage efficiency for the 18 Ω case as a representative operating-point analysis. While the baseline of physics-based PTO model tracks the qualitative dependence of efficiency on RPM—effectively reproducing the primary electromechanical coupling—it remains overly optimistic near and above the rated speed, consistent with the loss-proxy trends shown in Fig. 16.

While the present baseline model employs a lumped constant efficiency, similar to other time-domain studies [37], it currently lacks empirical calibration for the aforementioned velocity-dependent mechanical drag and load-dependent electrical transmission losses. Consequently, it becomes progressively optimistic in these high-power, overspeed regions. This corroborates the comprehensive wave-to-wire study by Penalba and Ringwood [30], which demonstrated that idealized numerical models frequently over-predict power output by failing to capture these stage-by-stage complex energy losses. Rather than arbitrarily attributing this widening discrepancy to a single physical source, it must be recognized that the observed discrepancies are an aggregation of highly intertwined mechanical and electrical mechanisms not accounted for in a constant-parameter machine and rectifier representation. To address this limitation, explicitly decouple these effects, and identify the dominant source restricting power generation, Section 5 introduces a conservative loss-augmentation and parameter-sensitivity workflow. By executing a targeted numerical sensitivity analysis (detailed in Section 5.1), this approach incorporates effective parameter roll-off for the over-speed regime, thereby enhancing agreement at high operating points while preserving fidelity in the primary operating window.

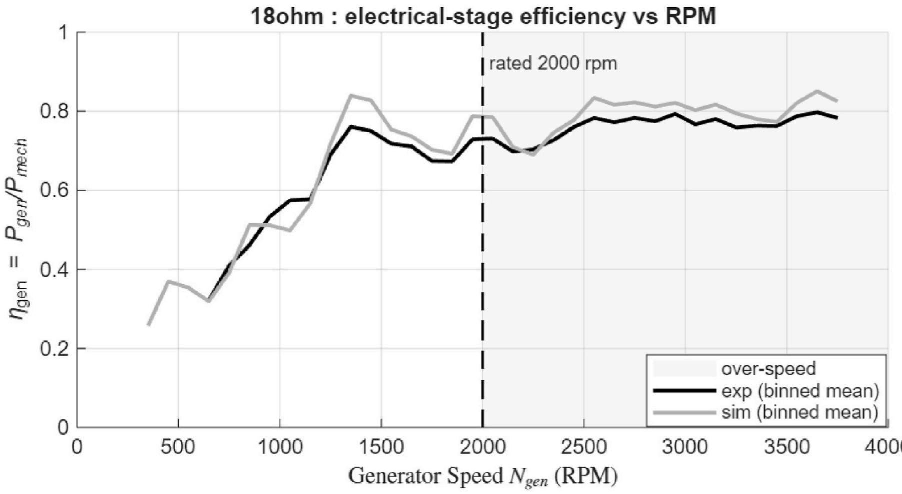

Fig. 17. Electrical-stage efficiency (η_{gen}) versus RPM for $R_L = 18\ \Omega$ (binned mean), comparing experiment and simulation. The dashed line indicates the rated speed (2000 rpm), and the shaded region denotes the over-speed diagnostic range.

5. Design-oriented discussion and forward projection

5.1. Design sensitivities and loss attribution along the energy cascade

As established in Section 4.3.2, the observed high-speed torque deviations are driven by coupled electromechanical non-idealities rather than basic restoring-force dynamics. The baseline model accurately captures the pretension system; across a 10 m stroke, accumulator pressure rises from 21 to 25 kg/cm^2, increasing pretension by 140 to 175 N. While critical for preventing line slack during rapid wave reversals, this contribution represents less than 8% of the payout tension and cannot explain the macroscopic over-predictions.

Executing the decoupling diagnostic analysis isolates the current-dependent discrepancies highlighted by the loss proxy. As shown in Fig. 18a, the simulation error is not merely a function of rotational speed, but is triggered by the electrical load state. Specifically, Fig. 18b reveals that the constant-parameter baseline model maintains high fidelity only when demanded current remains below the generator's rated limit of 5.16 A. Exceeding this threshold causes the prediction error (ΔI) to increase nonlinearly due to likely associated with armature reaction and magnetic saturation [38], which actively weaken the effective permanent magnet flux linkage. To accurately replicate this nonlinearity, the parameter sensitivity analysis empirically derived a current-dependent K_e derating trajectory, explicitly mapped in the best-fit K_e roll-off profile (Fig. 18e). As illustrated, the effective K_e raio relative to its nominal value progressively degrades once the stator current surpasses the 5.16 A boundary. Implementing this physics-informed parameter adjustment successfully neutralizes the high-current over-predictions, pulling the simulation error back to a zero-mean baseline (Fig. 18b).

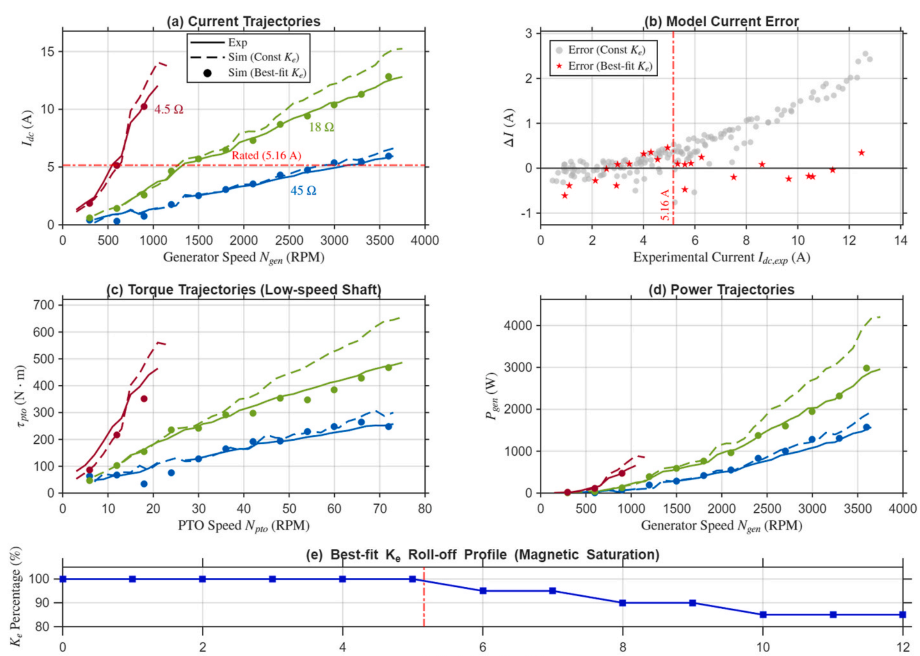

Fig. 18. Decoupling analysis of electromechanical nonlinearities under representative loads (45 Ω, 18 Ω, and 4.5 Ω). (a) DC current trajectories, highlighting simulation divergence above the 5.16 A rated limit. (b) Current prediction error (ΔI), contrasting the uncorrected constant K_e model against the best-fit K_e correction. (c) Low-speed shaft torque and (d) electrical power trajectories, demonstrating exceptional alignment between experimental data (solid lines) and the corrected non-linear simulation (markers). (e) The empirically derived best-fit K_e roll-off profile accounting for high-current magnetic saturation.

It is crucial to emphasize that the baseline model already incorporates a physics-based viscous rotational damper on the high-speed shaft. This damper is empirically calibrated via no-load tests (Fig. 11) to account for speed-dependent mechanical parasitic losses, such as oil churning and bearing windage. Because these mechanical non-idealities are successfully isolated and pre-compensated in the numerical setup, the persistent torque and power over-predictions observed under heavy electrical loads cannot be attributed to unmodelled drivetrain friction. Rather, the residual mismatch is primarily dominated by the aforementioned electromagnetic nonlinearities. As demonstrated in the corrected low-speed shaft torque (Fig. 18c) and electrical power trajectories (Fig. 18d), replacing the constant K_e assumption with the best-fit K_e roll-off profile effectively removes the systematic bias, yielding exceptional agreement across the entire energy cascade.

These decoupled findings provide a critical projection for real-world deployments: because electromechanical parameters roll off under extreme transient overloads, single-point static tuning is insufficient. Maximizing the full wave-to-wire potential necessitates parameter-scheduled control strategies. By dynamically adapting the electrical load to maintain the PTO within an optimal RPM and current band, future controllers can mitigate severe magnetic saturation while maximizing overall energy extraction.

5.2. Model limitations and projections for up-scaled design

A key finding from Section 5.1 is that a physics-based model initialized with supplier specifications still requires adequate land testing for proper calibration. Specifically, utilizing open-circuit crane trials isolated and calibrated the baseline mechanical losses, allowing the numerical model to accurately capture the no-load F_{line} over a long stroke and high V_{line}. However, the analysis also reveals that once a resistive load is introduced and the generator operates beyond its rated current limit, a constant K_e assumption is no longer valid. To maintain predictive accuracy under these heavy load conditions, a current-dependent K_e roll-off must be introduced to account for magnetic saturation.

While this calibration methodology provides a robust baseline, the limitations of the current experimental framework must be explicitly acknowledged. The physical land tests utilized continuous, long stroke crane motions to isolate quasi-steady payout and haul-in dynamics. Consequently, these linear, unidirectional strokes cannot fully represent the high-frequency periodic motions, rapid bidirectional reversals, and stochastic wave interactions characteristic of an actual wave energy converter operating in real ocean conditions.

Despite the lack of periodic wave excitation in the land tests, this validated onshore PTO framework establishes a structurally consistent foundation for future up-scaled designs. Because the model architecture relies on fundamental physical parameters rather than arbitrary performance maps, scaling the device to higher power ratings can be systematically adapted by updating subsystem specifications and recalibrating scale-sensitive parameters. Moving forward, this modular PTO representation can be directly coupled with hydrodynamic solvers to project full wave-to-wire performance under realistic irregular sea states, significantly reducing the empirical testing required during the design phase of up-scaled prototypes.

6. Conclusion

This study evaluates a novel 1 kW-scale, long-stroke winch-driven PTO designed to circumvent the stroke limitation and end-stop collision issues prevalent in conventional point absorber wave energy converters. By executing a comprehensive experimental matrix across resistive loads from 4.5 to 45 Ω, we mapped the system performance using a phase-resolved energy cascade framework. This stage-wise accounting revealed that while mechanical transmission efficiency remains robust, the electrical conversion efficiency is highly sensitive to the applied load, culminating in an optimal overall cascade efficiency near 18 Ω. Furthermore, physical trials validated the integrated restoring-force subsystem. The pneumatic accumulator successfully generated progressive pretension to prevent tether slack and effectively prevented tether slack and mitigated snap-load risk, even during aggressive haul-in phases reaching retraction velocities of 1.27 m/s.

A fundamental contribution of this work is the development of a physics-based PTO model that bridges supplier specifications with rigorous land test calibration. To accurately reflect real world dynamics, a decoupled calibration approach was implemented. First, open-circuit no-load crane trials were utilized to isolate and calibrate a lumped mechanical loss model, including high-speed rotational viscous damping, gearbox efficiency, and restoring interface friction. This allowed the numerical model to accurately predict the baseline line tension trajectory under long-stroke conditions. With mechanical parasitics confidently bounded, the model successfully diagnosed that power overpredictions under heavy electrical loads are driven by electromechanical nonlinearities, specifically magnetic saturation requiring a load-dependent back-EMF derating. Ultimately, this validated physics-based architecture establishes a structurally consistent foundation for future up-scaling. By eliminating the reliance on static empirical look-up tables, this modular PTO representation can be directly coupled with hydrodynamic solvers to develop dynamic, load-scheduled control strategies that maximize energy extraction while mitigating transient overloads in irregular seas.

CRediT authorship contribution statement

Wen-Yang Hsu: Conceptualization, Data curation, Formal analysis, Investigation, Methodology, Validation, Visualization, Writing – original draft. **Yi-Hsiang Yu:** Conceptualization, Formal analysis, Methodology, Software, Writing – review & editing. **Yu-Chi Chang:** Resources, Writing – review & editing. **Lei Zuo:** Conceptualization, Methodology, Writing – review & editing. **Yang-Chi Chung:** Investigation, Validation. **Bo-Han Wang:** Investigation, Validation.

Funding

This work was financially supported by the National Science and Technology Council of Taiwan under grant number 114-2221-E−019-040, and by the Energy Administration, Ministry of Economic Affairs, R. O.C., under grant number 112-D0311.

Declaration of competing interests

The authors declare that they have no known competing financial interests or personal relationships that could have appeared to influence the work reported in this paper.

References

[1] K. Gunn, C. Stock-Williams, Quantifying the global wave power resource, Renew. Energy 44 (2012) 296–304.
[2] IRENA, Innovation Outlook: Ocean Energy Technologies, International Renewable Energy Agency, Abu Dhabi, 2020.
[3] E. Al Shami, R. Zhang, X. Wang, Point absorber wave energy harvesters: a review of recent developments, Energies 12 (1) (2018).
[4] A. Abbasi, H. Ghassemi, A comparative state-of-the-art review of wave energy converters: point absorbers, linear absorbers, and hybrid systems, Appl. Energy 409 (2026) 127487.
[5] A. Sewter, S.P. Neill, The co-location of wind and wave energy at multiple global sites, Renew. Energy 255 (2025).
[6] G. Zhu, Z. Shahroozi, S. Zheng, M. Göteman, J. Engström, D. Greaves, Experimental study of interactions between focused waves and a point absorber wave energy converter, Ocean Eng. 287 (2023).
[7] X.F. Li, D. Martin, C.W. Liang, C.A. Chen, R.G. Parker, L. Zuo, Characterization and verification of a two-body wave energy converter with a novel power take-off, Renew. Energy 163 (2021) 910–920.
[8] H.T. Do, T.D. Dang, K.K. Ahn, A multi-point-absorber wave-energy converter for the stabilization of output power, Ocean Eng. 161 (2018) 337–349.

[9] J. Orszaghova, S. Lemoine, H. Santo, P.H. Taylor, A. Kurniawan, N. McGrath, W. Zhao, M.V.W. Cuttler, Variability of wave power production of the M4 machine at two energetic open ocean locations: Off Albany, Western Australia and at EMEC, Orkney, UK, Renew. Energy 197 (2022) 417–431.

[10] H. Gao, J. Xiao, Power capture and output of a three-degree-of-freedom wave energy converter with a parallel hydraulic cylinder system, Energy 340 (2025) 139213.

[11] S. Xu, S. Wang, C. Guedes Soares, Review of mooring design for floating wave energy converters, Renew. Sustain. Energy Rev. 111 (2019) 595–621.

[12] G. He, Z. Luan, W. Zhang, R. He, C. Liu, K. Yang, C. Yang, P. Jing, Z. Zhang, Review on research approaches for multi-point absorber wave energy converters, Renew. Energy 218 (2023) 119237.

[13] R. Ahamed, K. McKee, I. Howard, Advancements of wave energy converters based on power take off (PTO) systems: a review, Ocean Eng. 204 (2020).

[14] Y. Gao, X. Li, X. Chen, L. Wang, Extreme wave and storm surge characteristics in the southeastern coastal and offshore regions of China, Sci. Rep. 15 (1) (2025) 26915.

[15] D.-J.T. Doong, Cheng Han, Ying-Chih Chen, Jen-Ping Peng, Ching-Jer Huang, Statistical analysis on the long-term observations of typhoon waves in the Taiwan sea, J. Mar. Sci. Technol. 23 (6) (2015).

[16] J. Falnes, Ocean Waves and Oscillating Systems: Linear Interactions Including Wave-Energy Extraction, Cambridge University Press, 2002.

[17] S.J. Beatty, B. Bocking, K. Bubbar, B.J. Buckham, P. Wild, Experimental and numerical comparisons of self-reacting point absorber wave energy converters in irregular waves, Ocean Eng. 173 (2019) 716–731.

[18] G. Ivanov, Y. Wu, K.-T. Ma, Optimized mooring solutions for floating offshore wind turbines in harsh environments, Ocean Eng. 340 (2025).

[19] B. Guo, T. Wang, S. Jin, S. Duan, K. Yang, Y. Zhao, A review of point absorber wave energy converters, J. Mar. Sci. Eng. 10 (10) (2022).

[20] Z. Shahroozi, M. Göteman, J. Engström, Experimental investigation of a point-absorber wave energy converter response in different wave-type representations of extreme sea states, Ocean Eng. 248 (2022).

[21] A.l. Babarit, J. Hals, A. Kurniawan, T. Moan, J. Krokstad, Power absorption measures and comparisons of selected wave energy converters. ASME 2011 30th International Conference on Ocean, Offshore and Arctic Engineering, 2011, pp. 437–446.

[22] J. Sjolte, C. Sandvik, E. Tedeschi, M. Molinas, Exploring the potential for increased production from the wave energy converter lifesaver by reactive control, Energies 6 (8) (2013) 3706–3733.

[23] J. Chapman, D. Perez-Torres, A. Baldini, J.B. Le Dreff, I. Masters, G. Foster, G. Stockman, D. Greaves, G. Iglesias, Validation of storm load limitation of a novel wave energy converter using scale model testing. Proceedings of the 12th European Wave and Tidal Energy Conference (EWTEC2015), 2017. Cork, Ireland.

[24] M. Lehmann, R. Elandt, H. Pham, R. Ghorbani, M. Shakeri, M.R. Alam, An artificial seabed carpet for multidirectional and broadband wave energy extraction: theory and experiment. Proceedings of the 10th European Wave and Tidal Energy Conference (EWTEC2013), 2013. Aalborg, Denmark.

[25] T.R. Mundon, B.J. Rosenberg, J. van Rij, Reaction body hydrodynamics for a multi-dof point-absorbing WEC. Proceedings of the 12th European Wave and Tidal Energy Conference (EWTEC2015), 2017. Cork, Ireland.

[26] M. Dragić, M. Hofman, V. Tomin, V. Miškov, Sea trials of sigma wave energy converter – power and efficiency, Renew. Energy 206 (2023) 748–766.

[27] D. Salar, A. Dupuis, J. Engström, E. Hultman, Emulating wave energy converter operation in irregular waves using a robotized dry test rig, Appl. Ocean Res. 166 (2026).

[28] J.C.C. Henriques, R.P.F. Gomes, L.M.C. Gato, A.F.O. Falcão, E. Robles, S. Ceballos, Testing and control of a power take-off system for an oscillating-water-column wave energy converter, Renew. Energy 85 (2016) 714–724.

[29] J.F. Gaspar, M. Calvário, M. Kamarlouei, C.G. Soares, Design tradeoffs of an oil-hydraulic power take-off for wave energy converters, Renew. Energy 129 (2018) 245–259.

[30] M. Penalba, J.V. Ringwood, A high-fidelity wave-to-wire model for wave energy converters, Renew. Energy 134 (2019) 367–378.

[31] X. Yue, D. Geng, Q. Chen, Y. Zheng, G. Gao, L. Xu, 2-D lookup table based MPPT: another choice of improving the generating capacity of a wave power system, Renew. Energy 179 (2021) 625–640.

[32] A.T. Asiikkis, D.G.E. Grigoriadis, A.I. Vakis, Wave-to-wire modelling and hydraulic PTO optimization of a dense point absorber WEC array, Renew. Energy 237 (2024).

[33] DNV, DNV-ST-0378, Standard for Offshore and Platform Lifting Appliances, DNV AS, 2021.

[34] I. American Petroleum, API RP 2D Operation and Maintenance of Offshore Cranes, 2014.

[35] The MathWorks, Inc, Simscape Version: Version 25.1, The MathWorks, Inc, Natick, Massachusetts, 2025. https://www.mathworks.com.

[36] L. Yang, J. Huang, S.J. Spencer, X. Li, J. Mi, G. Bacelli, M. Hajj, L. Zuo, Electrical power potential of a wave energy converter using an active mechanical motion rectifier based power take-off, Renew. Energy 252 (2025).

[37] R. Ali, M. Meek, B. Robertson, Submerged wave energy converter dynamics and the impact of PTO-mooring configuration on power performance, Renew. Energy 243 (2025).

[38] P.C. Krause, O. Wasynczuk, S.D. Sudhoff, Analysis of Electric Machinery and Drive Systems, IEEE Press, Wiley, 2013.